Journal of Catalysis 285 (2012) 103–114

Contents lists available at SciVerse ScienceDirect

Journal of Catalysis

journal homepage: www.elsevier.com/locate/jcat

Synergy between tungsten and palladium supported on titania for the catalytic total oxidation of propane

Marie N. Taylor [a], Wu Zhou [b], Tomas Garcia [c,*], Benjamin Solsona [d], Albert F. Carley [a], Christopher J. Kiely [b], Stuart H. Taylor [a,*]

[a] *Cardiff Catalysis Institute, School of Chemistry, Cardiff University, Main Building, Park Place, Cardiff CF10 3AT, UK*
[b] *Department of Materials Science and Engineering, Lehigh University, 5 East Packer Avenue, Bethlehem, PA 18015-3195, USA*
[c] *Instituto de Carboquímica (ICB-CSIC), C/Miguel Luesma, 50018 Zaragoza, Spain*
[d] *Departament d'Enginyeria Química, Universitat de València, C/Dr. Moliner 50, 46100 Burjassot, Valencia, Spain*

ARTICLE INFO

Article history:
Received 7 June 2011
Revised 13 September 2011
Accepted 16 September 2011
Available online 20 October 2011

Keywords:
Catalytic oxidation
Propane
Tungsten
Palladium
Palladium oxide
Titania
Aberration-corrected electron microscopy

ABSTRACT

Titania-supported palladium catalysts modified by tungsten have been tested for the total oxidation of propane. The addition of tungsten significantly enhanced the catalytic activity. Highly active catalysts were prepared containing a low loading of 0.5 wt.% palladium, and activity increased as the tungsten loading was increased up to 6 wt.%. Catalysts were characterised using a variety of techniques, including powder X-ray diffraction, laser Raman spectroscopy, X-ray photoelectron spectroscopy, temperature-programmed reduction and aberration-corrected scanning transmission electron microscopy. Highly dispersed palladium nanoparticles were present on the catalyst with and without the addition of WO_x. However, the addition of WO_x slightly increases the average palladium particle size, and there was some evidence for the Pd forming epitaxial islands on the support in the tungsten-doped samples. Surface analysis identified a combination of Pd^0 and Pd^{2+} on a Pd/TiO_2 catalyst, whereas all of the Pd loading was found in the form of Pd^{2+} with the addition of tungsten into the catalysts. At low tungsten loadings, isolated monotungstate and some polytungstate species were highly dispersed over the titania support. The concentration of polytungstate species increased as the loading was increased, and it was also promoted by the presence of palladium. The coverage of the highly dispersed tungstate species over the titania also increased as the tungsten loading increased. Some tungstate species were also found to be associated with the palladium oxide particles, and there was an enrichment of oxidised tungsten species at the peripheral interface of the palladium oxide nanoparticles and the titania. Sub-ambient temperature–programmed reduction experiments identified an increased concentration of highly reactive species on catalysts with palladium and tungsten present together, and we propose that the new WO_x-decorated interface between PdO_x and TiO_2 particles may be responsible for the enhanced catalytic activity in the co-impregnated catalysts.

1. Introduction

Catalytic total oxidation has been widely used for the abatement of dilute volatile organic compounds (VOCs), which are present in a wide variety of gaseous emissions, such as those arising from petrochemical processes, manufacturing plants and the treatment of solid and liquid wastes. Catalytic oxidation offers significant advantages over alternative VOC abatement technologies. For example, the operating temperature is lower than for thermal combustion, and hence, operating costs are lower as less supplementary fuel is required to achieve VOC removal. Furthermore, catalytic oxidation has the ability to treat VOCs in very dilute effluent streams [1].

Many different catalysts, as bulk metal oxides or perovskites [2,3], have been studied for the total oxidation of VOCs. However, it is generally accepted that supported noble metal catalysts, containing palladium or platinum, are the most active catalysts for the combustion of hydrocarbons [4,5]. Moreover, palladium-supported catalysts have been demonstrated to be more active for the total oxidation of short chain alkanes [6]. The behaviour of these supported palladium catalysts are strongly affected by the nature of the support. Although γ-Al_2O_3 has been extensively used as a support, mainly due to its low manufacturing cost [7], various studies [8–10] have shown that the use of other metal oxide supports, such as TiO_2, ZrO_2, SiO_2 and SnO_2, has resulted in more active catalysts for the oxidation of hydrocarbons. In addition, other positive effects have also been reported [11]; for example, TiO_2 is known to be more resistant to sulphur poisoning than Al_2O_3. It is generally

---

* Corresponding authors.
E-mail addresses: tomas@icb.csic.es (T. Garcia), taylorsh@cardiff.ac.uk (S.H. Taylor).

0021-9517/$ - see front matter © 2011 Elsevier Inc. All rights reserved.
doi:10.1016/j.jcat.2011.09.019

accepted that the catalytic total oxidation of hydrocarbons over palladium-supported catalysts proceeds by the reduction and oxidation cycle of palladium with the oxygen species originating from PdO species [12–14]. Thus, it is likely that the performance of the catalyst is related to the nature of the support through the dispersion of Pd and the Pd-support interaction [15].

The activity of supported catalysts may be modified by the presence of a second active component. Modifiers are generally added to promote activity and enhance resistance to deactivation. Vanadium [8,16], tungsten [17,18], niobium [19], cobalt [20], cerium [21] and lanthanum [22] have all been used, and they are known to promote the activity of supported metal catalysts for the oxidation of various VOCs. The positive promoting role of the different components mentioned above, for the oxidation of short chain alkanes, has generally been attributed to a range of different factors, such as controlling the noble metal particle size, catalyst reducibility and metal oxidation state.

In this work, we have extended previous studies of high-activity titania-supported palladium catalysts modified by vanadium [8] and niobium [23], by probing the effect of modifying the supported palladium catalyst with tungsten. It has been reported previously that doping W^{6+} cations into the crystalline structure of the TiO_2 support, prior to palladium impregnation, has a positive effect on the activity of Pd catalysts for benzene and ethyl acetate total oxidation [18]. However, we report here the first data available on co-impregnated tungsten-containing Pd/TiO_2 catalysts for the total oxidation of a short chain alkane. We have focused on probing the activity for the complete oxidation of propane, because short chain alkanes are emitted from a wide range of sources and they are recognised as some of the most difficult VOCs to oxidise [12]. In particular, we have explored the role of tungsten and palladium loading in the performance of these catalysts and develop a structural catalyst model to rationalise catalyst performance for propane total oxidation.

2. Experimental

2.1. Catalyst preparation

Catalysts with different chemical compositions of $Pd_x/W_y/TiO_2$ were prepared by a wet impregnation technique. A known amount of palladium(II) chloride (Aldrich, 99%) was dissolved in a minimum amount of hot de-ionised water (~10 ml/g). The solution was then heated to 80 °C, with continuous stirring, followed by the addition of an appropriate amount of tungstic acid. Titanium dioxide (~5 g, Degussa P25. $SA_{BET} = 50\ m^2\ g^{-1}$) was added to the heated solution and stirred continuously at 80 °C to form a paste, which was dried in an oven at 110 °C for 24 h. The resulting solid was ground in a pestle and mortar and calcined in static air at 550 °C for 6 h.

2.2. Catalyst characterisation

Catalyst surface areas were determined by multi-point N_2 adsorption at 77 K, and the data were treated in accordance with the BET method. Powder X-ray diffraction (XRD) was used to identify the crystalline phases present in the catalysts. An Enraf Nonius FR590 sealed tube diffractometer was used, employing Cu $K_{\alpha 1}$ X-rays (40 kV and 30 mA). XRD patterns were calibrated against a silicon standard and phases were identified by matching experimental patterns to the JCPDS powder diffraction file. The average crystallite size was determined from the diffraction peak broadening, relative to a highly crystalline silicon standard, by using the Scherrer equation [24].

A Renishaw system 1000 dispersive laser Raman microscope was used for recording Raman spectra. The excitation source used was an argon ion laser (514.5 nm) operated at a power of 20 mW. The laser was focused on powdered samples placed on a microscope slide to produce a spot size *ca.* 3 μm in diameter. A backscattering geometry with an angle of 180° between illuminating and collected radiation was used for recording data.

Temperature-programmed reduction (TPR) was performed using a micromeritics Autochem 2910 apparatus with a thermal conductivity detector. The reducing gas used was 10% H_2 in argon with a total flow rate of $50\ ml\ min^{-1}$. The temperature range explored was from room temperature to 900 °C with a heating rate of $10\ °C\ min^{-1}$. Sub-ambient TPR was carried out on 100 mg of catalyst, which was pretreated by heating from room temperature to 120 °C at a ramp rate of $20\ °C\ min^{-1}$ in flowing 10% O_2/Ar ($50\ ml\ min^{-1}$). The sample was maintained at 120 °C under O_2/Ar for 1 h, before being cooled under Ar to −100 °C. TPR was performed from −100 °C to 120 °C under 10% H_2/Ar at a flow of $50\ ml\ min^{-1}$ at a ramp rate of $20\ °C\ min^{-1}$.

Palladium particle sizes for the unpromoted catalysts were determined by pulsed CO chemisorption at 35 °C using an Ar flow of $20\ ml\ min^{-1}$ and pulses of 0.2 ml of 10% CO in Ar. Prior to CO uptake determination, all samples were treated under flowing hydrogen ($50\ ml\ min^{-1}$) at 400 °C and then flushed by Ar ($20\ ml\ min^{-1}$) for 60 min. In order to calculate the Pd particle size, an adsorption stoichiometry of Pd/CO = 1 was assumed, as this value has been widely used, and we are most interested in determining the trend of dispersion. Spherical particles were also assumed.

X-ray photoelectron spectroscopy (XPS) measurements were taken using a Kratos Axis Ultra DLD spectrometer using monochromatised Al Kα radiation, and analyser pass energies of 160 eV (survey scans) or 40 eV (detailed scans). Binding energies are referenced to the C(1s) peak from adventitious carbonaceous contamination, assumed to have a binding energy of 284.7 eV.

Ammonia temperature-programmed desorption (TPD) profiles were obtained using a fixed bed flow system equipped with a thermal conductivity detector. One-hundred milligrams of each catalyst was pretreated in flowing Ar at 500 °C for 6 h and then cooled down to 125 °C under vacuum. The samples were treated for 4 h with a flow of 1.3 kPa NH_3/Ar, and the weakly adsorbed NH_3 was removed by evacuation at 125 °C for 1 h. The NH_3-TPD profiles were obtained by heating at $5\ °C\ min^{-1}$ up to 600 °C under a $30\ ml\ min^{-1}$ flow of helium.

The microstructures of the supported Pd/TiO_2 and $Pd/WO_x/TiO_2$ catalysts were studied using high-angle annular dark-field (HAADF) imaging in an aberration-corrected scanning transmission electron microscope (STEM), which is also known as *Z*-contrast imaging. Samples suitable for STEM imaging were prepared by dipping a 300-mesh copper TEM grid, coated with a lacy carbon film, into the dry catalyst powder and then shaking off any loosely bound residue. STEM–HAADF imaging was performed on a 200 kV JEOL 2200FS (S)TEM equipped with a CEOS probe C_s-corrector. Typically, a ~1 Å (FWHM) coherent electron beam with ~30 pA probe current was used for imaging, and dwell times between 48 μs and 60 μs per pixel were applied. The HAADF images presented have been low-pass filtered to reduce background noise. Simultaneous HAADF and STEM–XEDS (X-ray energy dispersive spectroscopy) spectrum imaging experiments were performed on the same instrument with a ~100 pA electron probe and 2 s per pixel dwell time.

2.3. Catalyst activity

Catalytic activity was measured using a fixed bed laboratory micro-reactor. For each experiment, 50 mg of powdered catalyst was placed in a 1/4 in. o.d. stainless steel reactor tube. The reactor feed contained 5000 vppm propane in air with a total flow rate of 50 ml min^{-1}. Catalysts were packed to a constant volume to give a gas hourly space velocity (GHSV) of 45,000 h^{-1}. The reactants and products were analysed by online gas chromatography with a thermal conductivity and flame ionisation detector. The 100–400 °C temperature range was explored, and the reaction temperature was measured using a thermocouple placed in the centre of the catalyst bed. During reaction, the temperature measured within the catalyst bed was consistent with the temperature of the external heating furnace, indicating that there was no significant measureable exotherm within the catalyst bed. The differences between the inlet and outlet concentrations were used to calculate conversion data, and all carbon balances were in the range 100 ± 10%. Analyses were made at each temperature until steady-state activity was attained, and three analyses were taken and data averaged. Blank experiments were conducted in an empty reactor and showed negligible activity over the temperature range used in this study.

3. Results and discussion

3.1. Catalyst performance

The only reaction product observed for palladium-containing catalysts was CO_2. In the case of W/TiO_2 catalysts, CO_2 was the major reaction product, although propylene was also detected, but only at temperatures where conversion was relatively low and selectivity to propylene did not exceed 10%.

Fig. 1 depicts propane conversion as a function of reaction temperature for tungsten-free and tungsten-containing $0.5Pd/TiO_2$ catalysts. The activities of the catalysts containing tungsten were higher than those for the tungsten-free catalyst. Moreover, the activity increased as the tungsten loading of the catalyst increased. Tungsten loadings were limited to 6 wt.% as this is close to the theoretical monolayer, and as discussed later, it is known that above monolayer coverage, less active three-dimensional crystallites of WO_3 are formed. Clearly, the presence of tungsten in the Pd/TiO_2 catalyst greatly increased the catalytic combustion of propane at all temperatures. In fact, the $Pd–W/TiO_2$ catalysts all showed complete propane conversion to CO_2 at *ca.* 375 °C. This enhancement of activity is not the result of the additive effect of tungsten and palladium, since the activity of W/TiO_2 catalysts is very low, as they are almost inactive at 400 °C. Thus, these data clearly show that there is a synergistic effect between TiO_2-supported palladium and tungsten for the catalytic total oxidation of propane.

Fig. 2 compares the catalytic performance of Pd/TiO_2 and tungsten-promoted Pd/TiO_2, for various palladium loadings, at a constant tungsten content of 3 wt.%. The catalytic activity for the tungsten-promoted Pd/TiO_2 catalysts increased as the palladium content was increased. In the case of the W-free catalysts, the activity was very similar regardless of the Pd content, indicating that the activity per palladium content decreases when the Pd loading increases.

A summary of catalytic activity is presented in Table 1, where T_{10}, T_{50} and T_{90}, the reaction temperatures for alkane conversions of 10%, 50% and 90%, respectively, are shown. The most active catalyst was $0.5Pd–6.0W/TiO_2$, which had a much higher activity than the tungsten-free $0.5Pd/TiO_2$ catalyst. It is clear that the simple one step co-impregnation method of introducing palladium and tungsten onto the TiO_2 support significantly increases the activity of the catalysts.

3.2. Catalyst characterisation

A summary of the physical characteristics of the catalysts prepared is shown in Table 2. The surface area of the titania support was 50 $m^2 g^{-1}$, and this was reduced slightly by the addition of palladium and tungsten as expected. This can be attributed to the filling of the pores of the titania support as the impregnated species were added. CO chemisorption was employed to determine the palladium particle size on the surface of the unpromoted catalysts. As expected, larger average particle sizes of palladium were formed when the Pd content was increased (Table 2).

The XRD patterns obtained from $Pd–WO_x/TiO_2$ catalysts with different tungsten and palladium loadings are shown in Figs. 3 and 4. For comparative purposes, Fig. 4 also presents the XRD pattern for Pd/TiO_2 catalysts having different Pd loadings. The main crystalline phases identified correspond to the anatase and rutile phases of TiO_2 with anatase being predominant. The relative proportions of the crystalline titania phases were not modified by the addition of palladium and tungsten. Furthermore, there was no modification of titania crystallite size or change of microstrain. No diffraction peaks corresponding to any tungsten-containing crystalline phases were identified. This could be attributed to its presence at very low concentrations and the nature and high dispersion of the tungsten species. However, diffraction peaks from PdO with a characteristic reflection at 33.9° (JCPDS: 85-0624) were identified in the palladium-containing catalysts. The intensity of

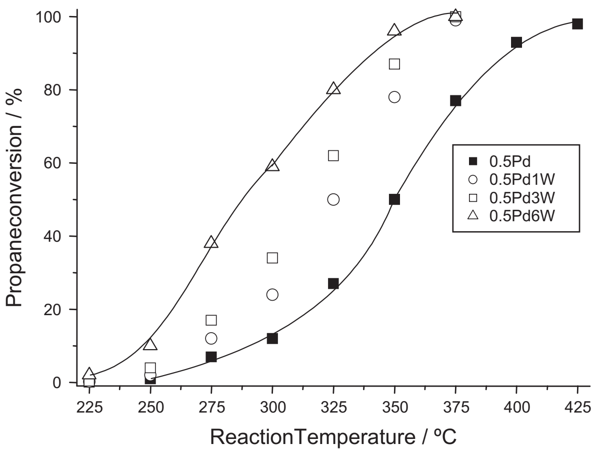

Fig. 1. Propane conversion at different temperatures for W-promoted Pd/TiO_2 catalysts with varying tungsten loading and constant palladium loading. (□) $0.5Pd/TiO_2$, (■) $0.5Pd–1W/TiO_2$, (+) $0.5Pd–2W/TiO_2$, (▲) $0.5Pd–3W/TiO_2$, (×) $0.5Pd–6W/TiO_2$.

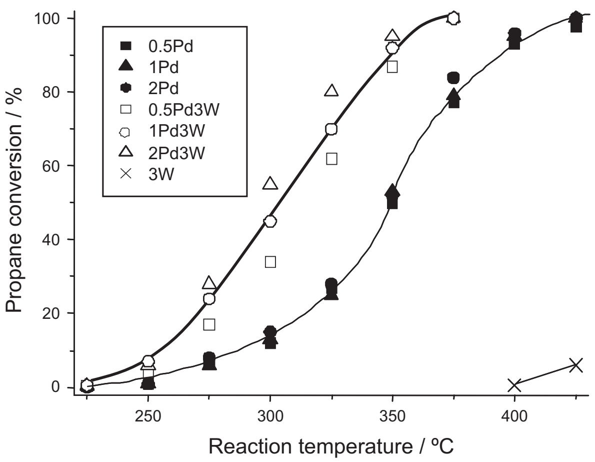

Fig. 2. Propane conversion at different temperatures for W-promoted Pd/TiO_2 catalysts, with constant tungsten loading and varying palladium loading. (□) $0.5Pd/TiO_2$, (○) $3W/TiO_2$, (▲) $0.5Pd–3W/TiO_2$, (▼) $1Pd–3W/TiO_2$, (●) $2Pd–3W/TiO_2$.

Table 1
Catalytic performance of Pd-, W- and Pd/W–TiO_2 catalysts for propane total oxidation, expressed in terms of the temperatures required for 10%, 50% and 90% conversion.

Catalyst	T_{10} (°C)	T_{50} (°C)	T_{90} (°C)[i]
0.5Pd/TiO_2	280	350	395
1Pd/TiO_2	280	345	395
2Pd/TiO_2	280	350	390
3W/TiO_2	430	–	–
6W/TiO_2	425		
0.5Pd/1W/TiO_2	270	330	365
0.5Pd/2W/TiO_2	270	325	360
0.5Pd/3W/TiO_2	265	315	355
0.5Pd/6W/TiO_2	250	290	340
1.0Pd/3W/TiO_2	260	305	350
2.0Pd/3W/TiO_2	255	295	345

the PdO peaks was significantly higher in tungsten-promoted catalysts when compared to those materials without tungsten. The intensity of the PdO peak also increased with both increasing palladium and tungsten content (Figs. 3 and 4). The Scherrer equation was used to estimate the average particle sizes of the PdO nanocrystals in some of the tungsten-promoted Pd/TiO_2 catalysts. These data are reported in Table 2. It was observed that the average palladium oxide particles in tungsten-free catalysts were smaller than those in the Pd–WO_x/TiO_2 catalysts, as values of ≈3–6 nm were measured in the former as compared to ≈6–10 nm in the latter. It is worth highlighting that when increasing the tungsten loading at 0.5 wt.% palladium, the reflection corresponding to the Pd–O nanocrystals can be much more clearly identified. This is associated with a lower dispersion of the PdO nanocrystals, since the total oxidation of the palladium species to PdO is observed for all the Pd–WO_x/TiO_2 catalysts (*qv post*). In addition, the palladium oxide average size increases with the palladium content for Pd–WO_x/TiO_2 catalysts. Finally, although the existence of metallic palladium is very likely in the tungsten-free samples, at least at the surface as shown by the XPS data, (*qv post*), diffraction peaks corresponding to bulk metallic palladium were not detected.

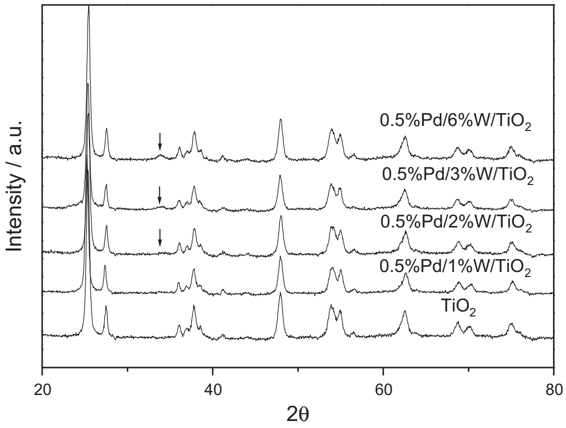

Fig. 3. Powder X-ray diffraction patterns for tungsten-promoted Pd/TiO_2 catalysts at different W loadings.

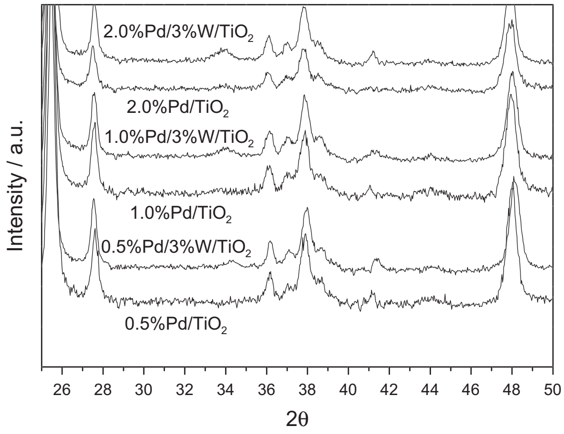

Fig. 4. Comparison of powder X-ray diffraction patterns for tungsten-promoted and unpromoted Pd/TiO_2 catalysts at different Pd loadings.

Fig. 5A presents a series of Raman spectra recorded from 300 to 1050 cm^{-1} for the tungsten/palladium catalysts. The main peaks were observed at *ca.* 650, 500 and 400 cm^{-1}, and these are typical of the anatase phase of TiO_2. Shoulders at *ca.* 450 and 790 cm^{-1} are also from anatase, and a shoulder at *ca.* 605 cm^{-1} can be ascribed to rutile [25]. Table 2 reports the Raman shifts and full width at half-maximum (FWHM) values for the 650 cm^{-1} anatase Raman band. The addition of either tungsten or palladium alone to the titania support did not modify significantly the relative intensities and position of the anatase TiO_2 bands, indicating that the anatase support was not affected by the deposition of tungsten or palladium. However, as detailed in Fig. 5B, the co-addition of tungsten and palladium to the titania displaces the anatase bands to lower frequencies by *ca.* 5 cm^{-1} and changes their shape. Both the shift in the position and the width of the TiO_2 Raman bands have been

Table 2
Physical characteristics of the catalysts studied in the present work.

Catalyst	Pd (wt.%)	W (wt.%)	Surface area ($m^2\,g^{-1}$)	Pd particle size[a,b] (nm)	Raman peak (FWHM)[c] (cm^{-1})
TiO_2	–	–	50	–	639 (29.5)
0.5Pd/TiO_2	0.5	–	46	3.4[b]	640 (29.4)
1Pd/TiO_2	1.0	–	44	5.2[b]	638 (29.7)
2Pd/TiO_2	2.0	–	45	6.1[b]	639 (29.7)
3W/TiO_2	–	3.0	48	–	640 (29.4)
6W/TiO_2	–	6.0	49	–	639 (28.9)
0.5Pd–1W/TiO_2	0.5	1.0	46	n.d.[a]	635 (35.2)
0.5Pd–2W/TiO_2	0.5	2.0	47	n.q.[a]	636 (32.4)
0.5Pd–3W/TiO_2	0.5	3.0	45	6[a]	636 (31.9)
0.5Pd–6W/TiO_2	0.5	6.0	48	8[a]	635 (32.3)
1Pd–3W/TiO_2	1.0	3.0	48	9[a]	635 (32.9)
2Pd–3W/TiO_2	2.0	3.0	49	10[a]	636 (34.6)

n.d.: not detected, n.q.: not quantified.

[a] By XRD.

[b] By CO chemisorption.

[c] Raman frequency and full width at half-maximum (FWHM) for the Eg band at 640 cm^{-1}.

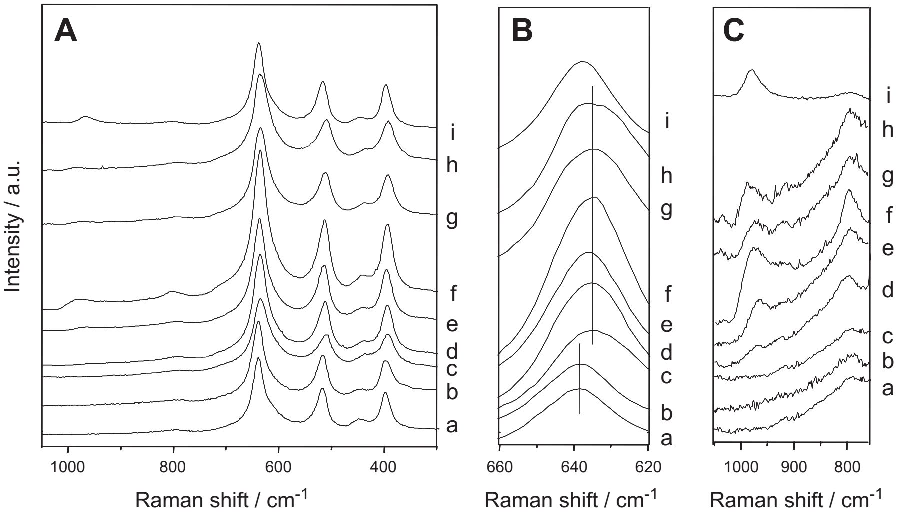

Fig. 5. Laser Raman spectra for Pd/W/TiO_2 catalysts. Catalysts: (a) TiO_2, (b) 0.5Pd/TiO_2, (c) 0.5Pd–1W/TiO_2, (d) 0.5Pd–2W/TiO_2, (e) 0.5Pd–3W/TiO_2, (f) 0.5Pd–6W/TiO_2, (g) 1Pd–3/TiO_2, (h) 2Pd–3W/TiO_2 and (i) 6W/TiO_2.

studied previously. Interpretation of the variation of Raman peak shapes have been attributed to a range of factors, such as (i) a pressure effect due to the surface tension of grains [26], (ii) a decrease in the Ti–O bond strength, (iii) non-stoichiometry as induced by oxygen deficiency or disorder induced by some minor phases in the sample [27], and (iv) phonon confinement effects with the grain size variation [28]. Since the difference in crystallite sizes and microstrain for Pd–WO_x/TiO_2 catalysts is not significant, and the same phases are detected for all the catalysts, we can tentatively conclude that the frequency shift and the FWHM increase of the 650 cm^{-1} anatase band, as the tungsten and palladium loading are varied, are primarily associated with the presence of more oxygen defects in the TiO_2 support. Consequently, a shift of charge density takes place, resulting in reduction of titanium and oxidation of palladium and/or tungsten in the Pd/W/TiO_2 catalysts.

Vibrations related to tungsten species can also be observed in the Raman spectra (Fig. 5C), although these bands exhibit lower intensity than those presented by the TiO_2. A broad band at around 980 cm^{-1}, which can be assigned to terminal W=O stretching modes corresponding to highly dispersed WO_x species, was detected [29]. As the tungsten loading increased, the band at *ca.* 980 also increased in intensity, indicating a progressive build-up of WO_x surface species. Accordingly, the shift to a higher wave number of this Raman band with higher tungsten surface density was attributed by Eibl et al. [30] to an increased polymerisation of tungsten species. Comparing the Raman spectra of the 6 wt.% W/TiO_2 catalysts with and without palladium (spectra f and i, respectively), it can be observed that the incorporation of palladium causes both a shift in the position of the vibrational band from 978 cm^{-1} to 996 cm^{-1}, and this is accompanied by a slight increase in intensity. Thus, the presence of palladium acts to increase the polymerisation of WO_x species.

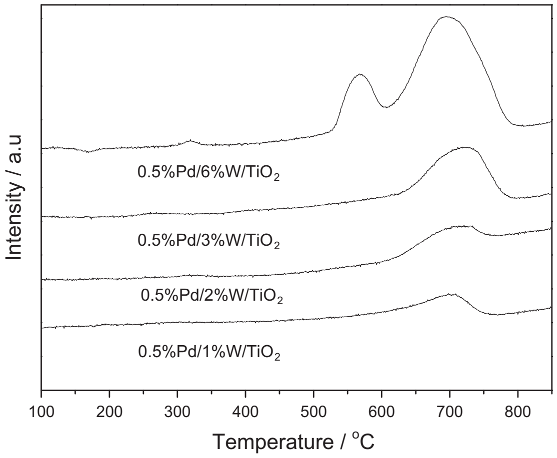

Fig. 6. Temperature-programmed reduction profiles for Pd/W/TiO_2 catalysts. Profiles for 0.5Pd–1W/TiO_2, 0.5Pd–2W/TiO_2, 0.5Pd–3W/TiO_2 and 0.5Pd–6W/TiO_2.

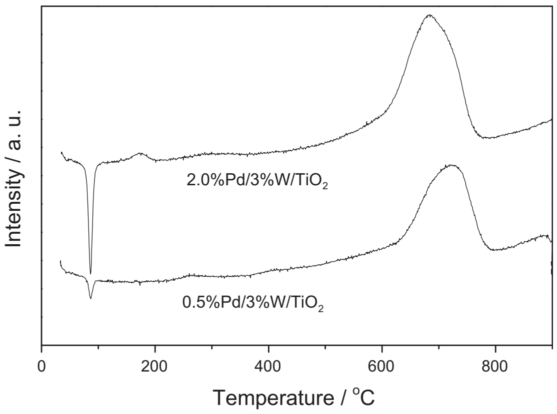

Fig. 7. Temperature-programmed reduction profiles for Pd–WO_x/TiO_2 catalysts. Profiles for 0.5Pd–3W/TiO_2 and 2Pd–3W/TiO_2.

Temperature-programmed reduction profiles up to 900 °C are shown in Figs. 6 and 7. These data mainly provide information on the influence of the palladium sites on the reducibility of the tungsten species. All the tungsten-containing catalysts showed a TPR peak at *ca.* 700 °C (Fig. 6), and there was a general increase in the total hydrogen consumption with the increase in tungsten loading. This suggests an increase in the amount of potential reducible species as the tungsten content was increased. The hydrogen reduction peak has been related to the reduction of W^{6+} to W^{4+} in the surface of the WO_x domains [31]. It is interesting to note that the TPR profiles are similar to those previously reported for WO_x/TiO_2 catalysts [31], although a reduction peak at *ca.* 550 °C was also observed for the palladium-containing catalyst with the highest tungsten loading. The lower temperature reduction peak exhibited by the most active 6.0% tungsten Pd/

TiO_2 sample was absent in the other catalysts. Fig. 7 demonstrates how the reduction of WO_x species is influenced by the palladium loading. The main WO_x reduction feature was shifted to a slightly lower temperature when the concentration of palladium was increased. The profile also shows a negative peak below 100 °C, which is distinctive for the decomposition of palladium hydride.

It is generally accepted that the main reduction peaks of palladium occur at sub-ambient temperatures [32]. Fig. 8 shows sub-ambient TPR profiles for a representative subset of catalysts in order to probe the reducibility and nature of palladium sites in more detail. The peaks observed at *ca.* 0 °C for tungsten-free Pd/TiO_2 catalysts can be assigned to the reduction of PdO_x to metallic palladium. Table 3 shows the H_2 consumption for these catalysts during the sub-ambient TPR experiments. For the tungsten-free Pd/TiO_2 catalysts, the H_2 consumption represents around 80% of the total theoretical reduction of PdO to Pd^0 and is in agreement with XPS data presented later. For tungsten-containing Pd catalysts, a peak, which can be deconvoluted into two peaks, appears at *ca.* 20 °C. The hydrogen consumption represents between 110% and 150% of the theoretical consumption for the reduction of PdO to Pd^0. Therefore, hydrogen consumption at *ca.* 20 °C must also be related to the reduction of new highly reducible species, which are only present on the catalyst when palladium and tungsten are present simultaneously.

Surface-sensitive XPS was used to investigate the oxidation state of the Pd species and any possible correlations with catalytic activity. For W-promoted Pd/TiO_2 catalysts, it was observed that the oxidation state of the palladium species is strongly influenced by the addition of tungsten to the Pd/TiO_2 catalysts (Fig. 9). For the pure 0.5 wt.% Pd/TiO_2 sample (Fig. 9a), the Pd exists as both metallic species and PdO particles, the intensity ratio indicating a composition of 40% Pd^0 and 60% Pd^{2+} [23]. This agrees with the hydrogen consumption obtained in the sub-ambient TPR experiments which indicate that a complete PdO → Pd° transition does not occur in tungsten-free catalysts. However, if tungsten is added at any concentration, the XP spectra show the complete absence of metallic Pd^0, the palladium being present purely as PdO (Fig. 9b–d).

The XP W(4f) spectra for the $Pd–W/TiO_2$ catalysts overlap strongly with the Ti(3p) signal from the titania support, and thus, the Ti(3p) spectrum from the tungsten-free catalyst must be subtracted from the composite signal. The methodology is shown in Fig. 10: the Ti(3p) signal from titania (curve a) is scaled appropriately and subtracted from the composite spectrum from the palladium–tungsten catalyst (curve b) to give the 'pure' W(4f) spectrum (curve c) which can then be quantified. The resulting W(4f) difference spectra indicate the presence of only 6+ species in the various palladium–tungsten and pure tungsten catalysts (Fig. 11).

Fig. 12 shows the ratio of the integrated W(4f) and Ti(2p) intensities against nominal tungsten loading; the excellent linear correlation is consistent with a high degree of dispersion of the W species for all loadings, including the palladium-free W/TiO_2 catalyst. These data also demonstrate that the titania support gets progressively more covered by surface WO_x species as the tungsten loading is increased.

The acidity of the catalysts was probed using NH_3-TPD, and results are shown in Fig. 13. Generally, the profile had a broad band with several maxima between 100 and 450 °C. The peaks correspond to different strengths of acid sites, weak acid sites (α) at *ca.* 150 °C, medium acid sites (β) at *ca.* 250 °C and strong acid sites (γ) at *ca.* 400 °C. It is apparent that the relative amount of the medium and strong acid sites is dependent on the palladium and tungsten loading. Thus, the number of β sites increases with the palladium loading and decreases with the tungsten loading. On the other hand, the number of γ sites, most likely related to polymeric tungsten species, increases with both the palladium

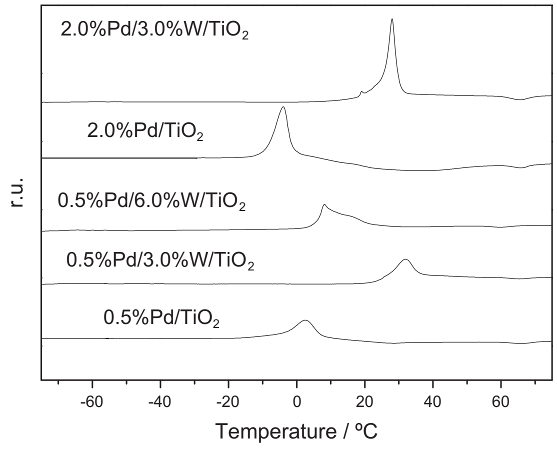

Fig. 8. Sub-ambient temperature-programmed reduction profiles for representative $Pd–WO_x/TiO_2$ catalysts.

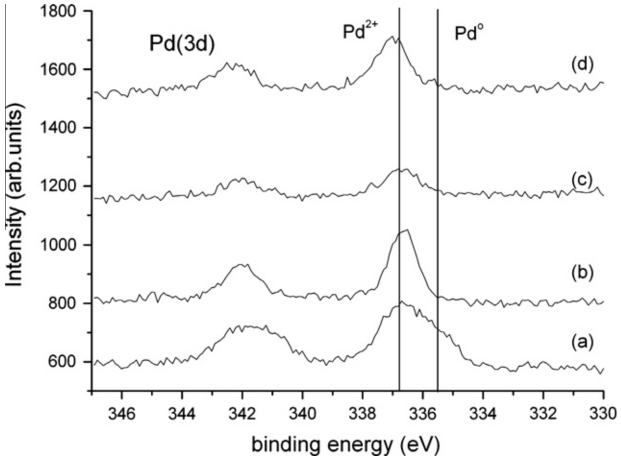

Fig. 9. Pd(3d) spectra for the W-doped 0.5 wt.% Pd/TiO_2 catalysts; W loadings are (a) 0 wt.%, (b) 1 wt.%, (c) 3 wt.% and (d) 6 wt.%.

Table 3
Hydrogen consumption during the sub-ambient temperature-programmed reduction experiments (μmol H_2/g).

Catalyst	T_{max} (°C)	H_2 consumption (μmol H_2 g^{-1})	H_2 consumed/H_2(PdO → Pd°) ratio[a]
$0.5Pd/TiO_2$	3	40	83
$2Pd/TiO_2$	−4	143	73
$0.5Pd–3W/TiO_2$	31	59	123
$0.5Pd–6W/TiO_2$	8	72	150
$2.0Pd–3W/TiO_2$	28	215	111

[a] H_2 consumed/H_2 consumed in the PdO → Pd transition, in%. Theoretical values in the case of complete reduction of Pd^{2+} to Pd^0 for catalysts containing 0.5 and 2.0 wt.% Pd are 48 and 194 μmol H_2/g, respectively.

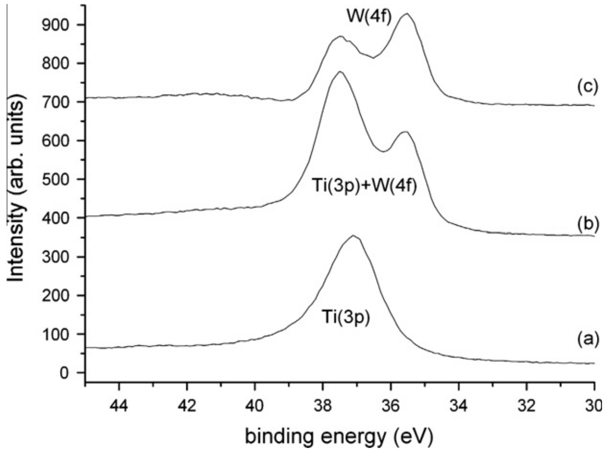

Fig. 10. Ti(3p) + W(4f) spectra for (a) the 0.5 wt.%Pd/TiO_2 catalyst, (b) the 0.5 wt.%Pd–3 wt.%W/TiO_2 catalysts and (c) the results of subtracting the Ti(3p) contribution from spectrum (b).

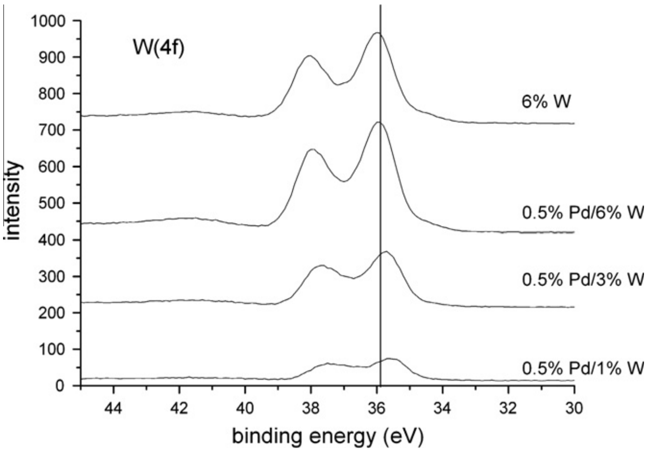

Fig. 11. W(4f) difference spectra for the W-doped Pd/TiO_2 catalysts, with W loadings as indicated.

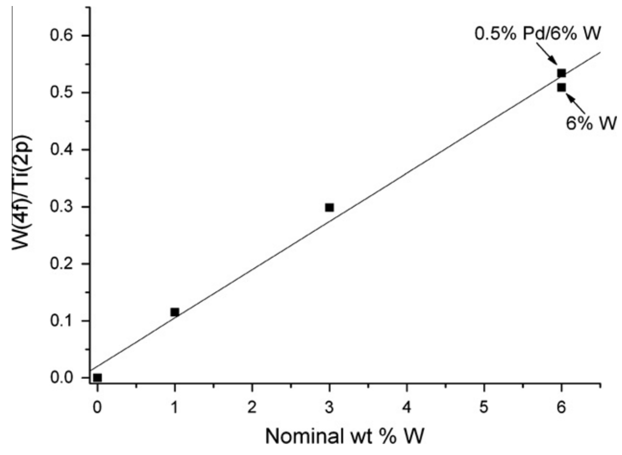

Fig. 12. Plot of the ratio of the intensities of the W(4f) and Ti(2p) spectra against nominal W loadings (wt.%) for the Pd–W catalysts, and the W-only sample.

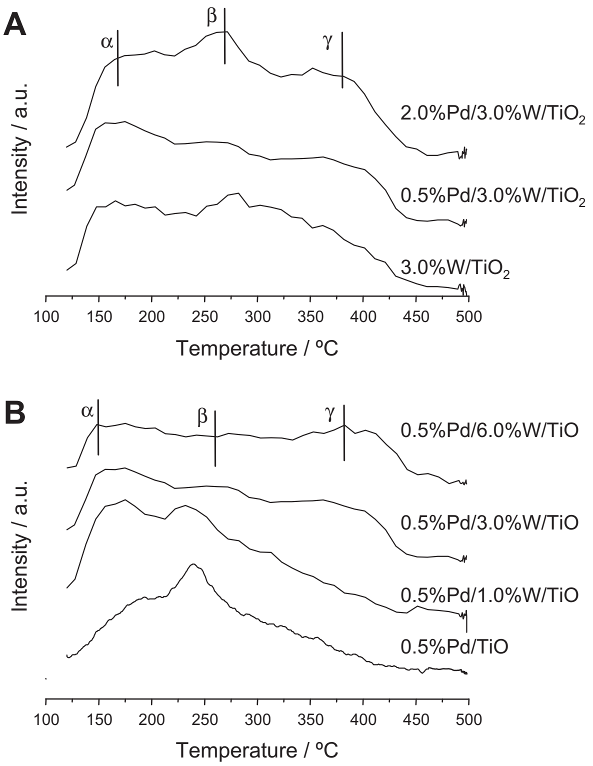

Fig. 13. Ammonia temperature-programmed desorption profiles for the different catalysts; (A) effect of palladium loading and (B) effect of tungsten loading.

Table 4
Total quantities of ammonia desorbed from temperature programmed desorption experiments.

Catalyst	Quantity of NH_3 desorbed (STP $cm^3\ g^{-1}$)
0.5Pd/TiO_2	3.85
3W/TiO_2	3.92
0.5Pd–1W/TiO_2	3.86
0.5Pd–3W/TiO_2	3.93
0.5Pd–6W/TiO_2	3.99
2.0Pd–3W/TiO_2	5.18

and the tungsten loading. In addition, the total number of catalyst acid sites, quantified from the total amount of NH_3 desorbed, increases with both the tungsten and the palladium loading. (Table 4). These data are in agreement with the findings from other studies on WO_x/TiO_2 catalysts [33,34]. These authors suggest that the total acidity of WO_x/TiO_2 catalysts increase with the tungsten oxide surface density at a surface coverage lower than the monolayer (<5 W nm^{-2}). Therefore, the NH_3-TPD data are in agreement with the results from other characterisation techniques, since we have observed an increasing amount of polymeric species due to increasing the WO_x loading and to the presence of palladium. There is no direct relationship between catalytic activity and the total acidity, since the catalyst with the highest acidity is not the most active. In addition, the marginal increase in the acidity of the bicomponent catalyst with increasing tungsten loading cannot alone account for the marked improvement of catalyst performance. Nevertheless, strong acidity could still be important, since the most active catalysts are those with the largest peaks at 400 °C in the NH_3-TPD profiles.

In order to probe the catalyst structure more fully, detailed electron microscopy studies have focussed primarily on the Pd/TiO_2 material and the most active 0.5Pd/6W/TiO_2 catalyst. Representative STEM–HAADF images from the simpler 0.5Pd/TiO_2 catalyst are shown in Fig. 14. In such Z-contrast images, the particles and atoms/atomic columns display bright contrast, with the contrast level proportional to $Z^{\sim 1.7}$. Due to the higher atomic number of

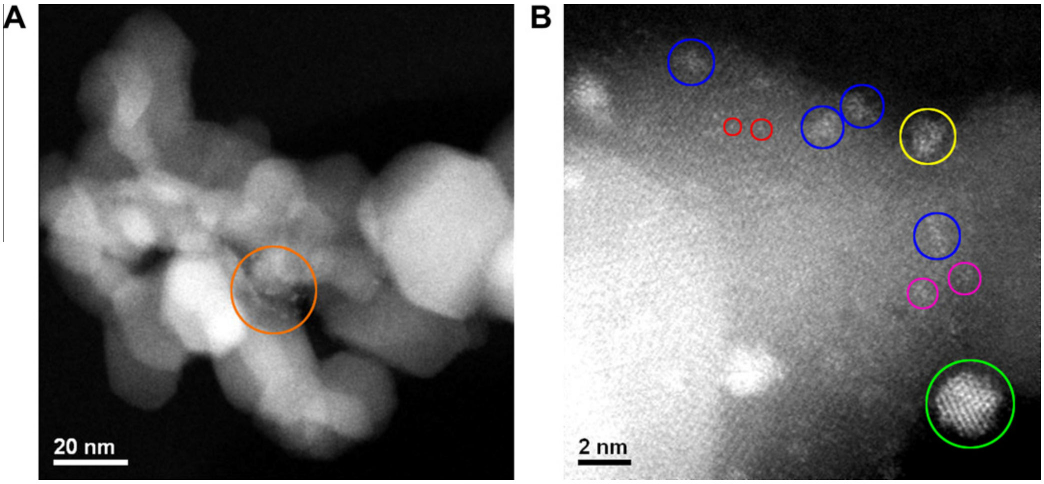

Fig. 14. Representative STEM–HAADF images for the 0.5% Pd/TiO_2 catalyst taken at different magnifications. The orange circle in (A) highlights the presence of PdO_x particles at the junction of TiO_2 support materials. The coloured circles in (B) indicate different PdO_x surface species found on TiO_2: red – isolated PdO_x monomer or single Pd atoms; purple – surface polymeric PdO_x species; blue – two-dimensional surface PdO_x rafts with dimensions of about 0.6- to 1.5-nm; yellow – 1- to 2-nm disordered PdO_x nanoparticles; green – 2- to 4-nm crystalline PdO_x particles. (For interpretation of the references to colour in this figure legend, the reader is referred to the web version of this article.)

Pd, compared with Ti and O, PdO_x species can be clearly identified *via* the positions of Pd atoms/atomic columns, which show higher image contrast against the TiO_2 support. As shown in the low magnification image (Fig. 14A), small PdO_x particles can be found on the TiO_2 surface at very low number density, and these small PdO_x particles tend to reside at the junctions of the TiO_2 support particles as highlighted in Fig. 14A. However, high-resolution HAADF images revealed the presence of at least five different PdO_x species in the sample. As shown in Fig. 14B: (i) isolated PdO_x monomer or single Pd atoms, (ii) polymeric PdO_x surface species formed by a few PdO_x units, (iii) two-dimensional surface PdO_x rafts with a size of about 0.6- to 1.5-nm, (iv) 1- to 2-nm disordered PdO_x nanoparticles and (v) 2- to 4-nm crystalline PdO_x particles can all be observed on the TiO_2 support surface, and these are highlighted by different coloured circles. Larger sized PdO_x particles were not observed in this sample, which is consistent with XRD and CO chemisorption results (Table 2). Although oxygen atoms associated with the surface PdO_x species cannot be directly observed from the HAADF images, XPS results (Fig. 9) suggest that these PdO_x species are not fully oxidised, and some of them consist of metallic Pd. Even though PdO_x nanoparticles were formed in this sample, it is important to note that a large fraction of the TiO_2 support surface remains uncovered by the PdO_x species. In contrast, we have recently shown that when WO_x alone is dispersed onto the surface of TiO_2, most of the TiO_2 surface sites would be expected to be covered by atomically dispersed surface WO_x species, before any three-dimensional WO_3 nanoparticles could be formed [35,36]. The coexistence of large areas on the bare TiO_2 surface and PdO_x particles in the tungsten-free catalysts suggests that PdO_x has a relatively low affinity for the TiO_2 support compared with WO_x. Moreover, the PdO_x nanoparticles found in the Pd/TiO_2 sample are randomly oriented with respect to the TiO_2 support grains, and no epitaxial structures were observed.

Representative STEM–HAADF images from the 0.5%Pd/6%WO_x/TiO_2 catalyst are shown in Fig. 15. In this sample, the WO_x species were found to be highly dispersed on the TiO_2 surface, mainly in the form of monotungstate (*i.e.* isolated WO_x units) and two-dimensional surface polytungstate species (highlighted in Fig. 15B and C), and this is consistent with the Raman data. Some small ~1 nm WO_x clusters were also observed on the TiO_2 surface. Previous studies suggested that the surface structure of supported metal oxide catalysts is strongly influenced by the wetting interaction between the two metal oxide components, and WO_x tends to have a strong affinity for TiO_2 surface sites [35,36]. The WO_x structure and dispersion observed in this co-impregnated sample are very similar to those reported for a supported WO_3/TiO_2 catalyst with a similar WO_3 loading [30,31], which suggests that the additional presence of PdO_x does not significantly affect the bonding between WO_x and TiO_2 surface sites.

The addition of WO_x, however, tends to decrease the dispersion of PdO_x on the TiO_2 surface and results in a very noticeable increase in the average PdO_x particle size. Crystalline PdO_x particles, 8–15 nm in size, were observed in this sample, whilst smaller PdO_x particles ~2–4 nm in size were also occasionally found. Smaller surface PdO_x species, *i.e.* isolated PdO_x and polymeric PdO_x species as highlighted in Fig. 14, may also coexist with surface WO_x species. However, the number density of these smaller PdO_x species would be expected to be much lower than in the sample without WO_x, as a large fraction of the palladium loading would be consumed by the larger PdO_x particles. Interestingly, the surface of the 2- to 4-nm PdO_x particles and the peripheral interface between these small PdO_x particles and the TiO_2 support are often found to be decorated with WO_x species, as highlighted in Fig. 15C.

The larger PdO_x particles found in the co-impregnated sample often display some epitaxial orientation relationship with respect to the TiO_2 support (Fig. 15D), which were not observed in the sample without WO_x addition (Fig. 14). The formation of these new epitaxial structures suggests that WO_x may well be present at the interface between PdO_x and TiO_2 particles and change the interaction between these two oxide components. In order to further test this hypothesis, STEM–XEDS mapping was performed on this sample (Fig. 16). The sum spectrum extracted from the spectrum image indicates the presence of PdO_x, WO_x and TiO_2 (the C and Cu signals come from the carbon-coated Cu TEM grid). Background subtraction was performed when extracting elemental maps, in order to remove the artefacts due to varying background signals associated with different sample thicknesses. The elemental maps obtained from the spectrum image are shown in Fig. 16C–E, which reveal the spatial distribution of the three oxide components. From the Pd map (Fig. 16C), it is clear that the Pd loading is mainly congregated into the resulting PdO_x nanoparticles which displayed the highest image contrast in the HAADF image (Fig. 16A). By comparing the W and Ti maps (Fig. 16D and E), one can notice that WO_x species are highly distributed over

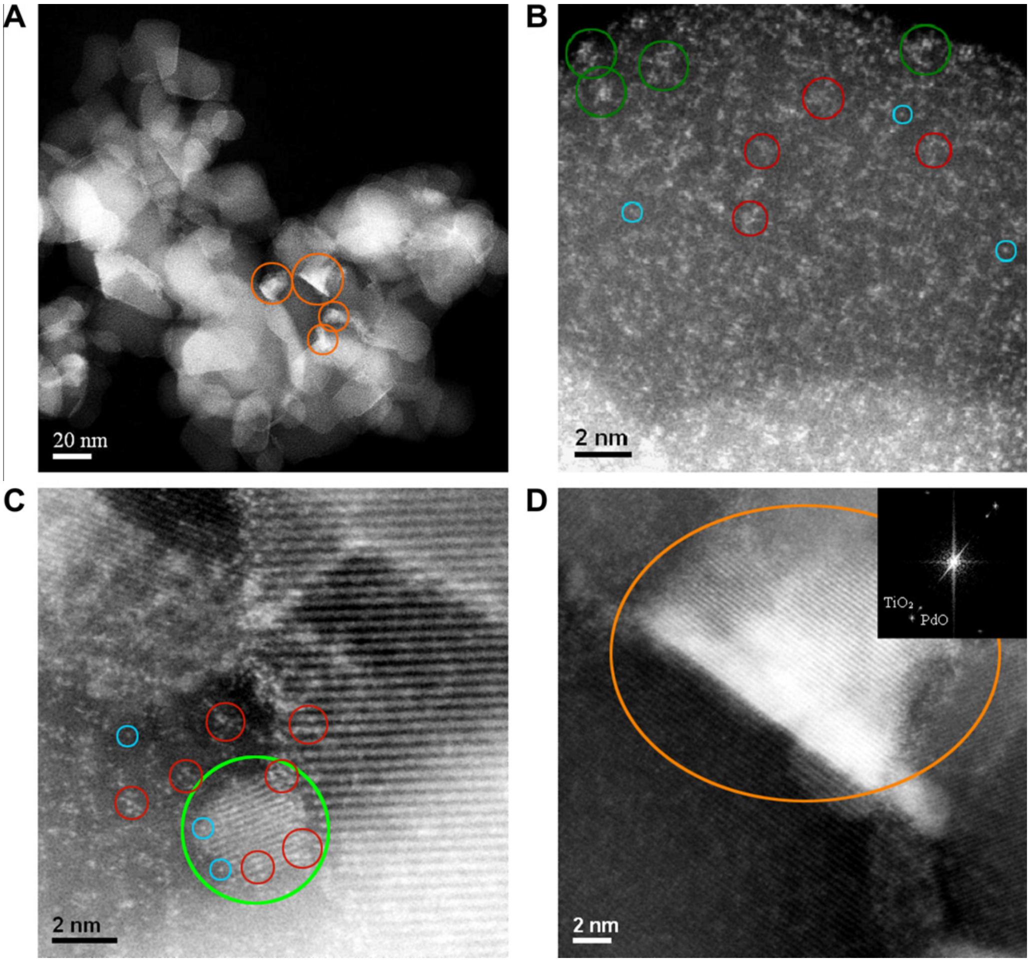

Fig. 15. Representative STEM–HAADF images for the 0.5Pd–6WO_x/TiO_2 catalyst. The various coloured circles indicate different surface species present on TiO_2: light blue – isolated WO_x (monotungstate); dark red – polymeric WO_x species (polytungstate); dark green – ~1 nm disordered WO_x clusters; green – 2- to 4-nm crystalline PdO_x particles; orange – 8- to 15-nm crystalline PdO_x particles. Inset: fast Fourier transform (FFT) of (D). The two diffraction spots correspond to tetragonal PdO (1 0 1) and rutile TiO_2 (1 1 0), respectively. (For interpretation of the references to colour in this figure legend, the reader is referred to the web version of this article.)

the entire surface of the TiO_2 particles, with some enhancement on the edge of the TiO_2 particles. By colour-coding the three elemental maps, we have reconstructed the relative spatial distribution of these three oxide components (Fig. 16F). Significantly, a noticeable increase in the W signal was observed at the interface/periphery of the PdO_x and TiO_2 particles (as indicated by the white arrows in Fig. 16F) as well as between adjacent PdO_x nanoparticles. This observation confirms that WO_x species are present at the junction between PdO_x and TiO_2 particles and may be promoting the formation of larger epitaxial structures between PdO_x and the TiO_2 support particles. High-resolution imaging and chemical mapping have been performed on supported metal catalysts; however, data of the resolution presented here are rare for supported metal oxide systems, and the *state-of-the-art* technique employed provides new insight to the structure of the catalysts.

3.3. Comments on the origin of improved catalytic activity

A degree of uncertainty persists around the effect of the noble metal particle size on hydrocarbon catalytic total oxidation. Some studies have not observed a correlation between activity and particle size [37], whilst others have identified a strong correlation [38]. Yazawa et al. [9] suggested that propane oxidation was affected by both palladium dispersion and oxidation state; however on a series of supports, the oxidation state was designated to be the dominant factor. Conversely, Hicks et al. [38] showed that highly dispersed palladium oxide was much less active than larger crystalline particles supported on alumina. In the present study, it was evident from chemisorption and X-ray line broadening data that the average palladium particle size was increased when tungsten was incorporated into the catalyst. This was confirmed by STEM analysis, which also showed that the average particle sizes measured by XRD and chemisorption are an over-simplification, as at least five palladium containing species were found to coexist, and these spanned a range of dimensions. Aberration-corrected electron microscopy data of this type, which show such a heterogeneous distribution of palladium, perhaps highlight why there is such disagreement over the relationship between particle size and activity. Although we observed that the more active catalysts containing tungsten have larger palladium particles, we do not consider this to be the predominant factor for controlling catalyst activity. For example, in W-free Pd/TiO_2 catalysts, the activity per palladium site decreases with increasing PdO crystallite size.

XPS was used to investigate the oxidation state of the near-surface palladium species. The palladium catalyst without tungsten had Pd^0 and Pd^{2+} species present, with ~40% in the metallic state and ~60% in the more oxidised state. Once tungsten was incorporated into the catalyst, the surface oxidation state of palladium was modified significantly, and only Pd^{2+} was identified in the fresh catalyst. It has been suggested that the palladium oxidation state is an important factor in determining hydrocarbon total oxidation activity and that partially oxidised palladium results in a more

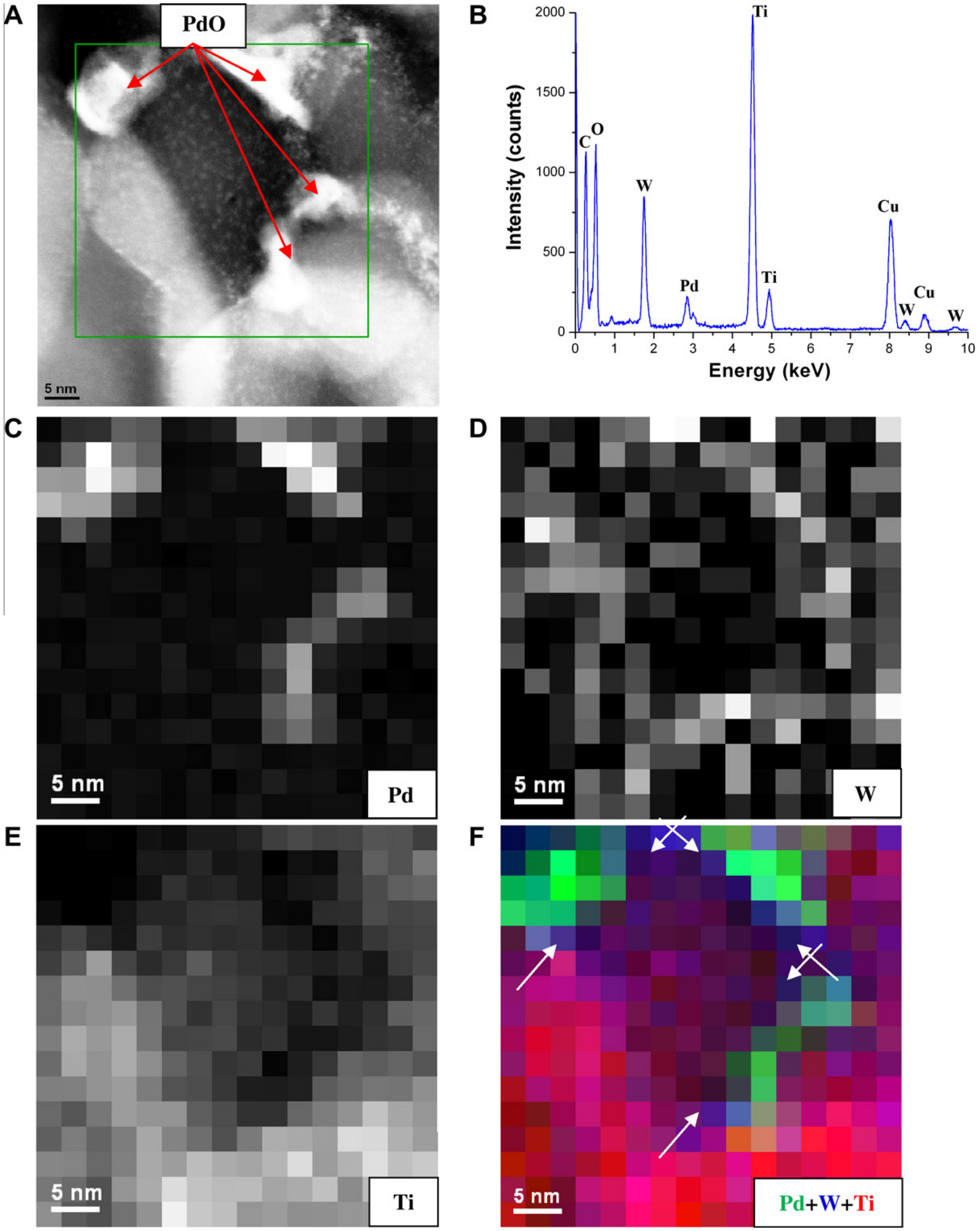

Fig. 16. STEM–XEDS spectrum imaging of the 0.5Pd–6WO$_x$/TiO$_2$ catalyst. (A) STEM–HAADF survey image. The green square indicates the area where the spectrum imaging was performed. (B) XEDS sum spectrum extracted from the spectrum image. (C) Background-subtracted Pd map. (D) Background-subtracted W map. (E) Background-subtracted Ti map. (F) Colour coded reconstruction map with Pd in green, W in blue and Ti in red. The white arrows in F indicate the peripheral interface between PdO$_x$ and TiO$_2$ particles, where an increase in W signal was observed. (For interpretation of the references to colour in this figure legend, the reader is referred to the web version of this article.)

active catalyst [9]. This is clearly not the case for these fresh Pd–WO$_x$/TiO$_2$ catalysts, as the Pd/TiO$_2$ material, which contained partially oxidised palladium, was less active than the tungsten-containing catalyst with fully oxidised palladium species. Furthermore, all the fresh catalysts containing tungsten only had Pd^{2+} present, and if the presence of partially oxidised palladium was controlling activity, the Pd^0/Pd^{2+} ratio would be expected to change as the amount of tungsten was increased, as this resulted in an increase in activity. These data and discussion are related to fresh unused catalysts, and it would be informative to consider the relative proportions of reduced and oxidised palladium on a used catalyst. Hence, XPS was carried out on a used sample of the most

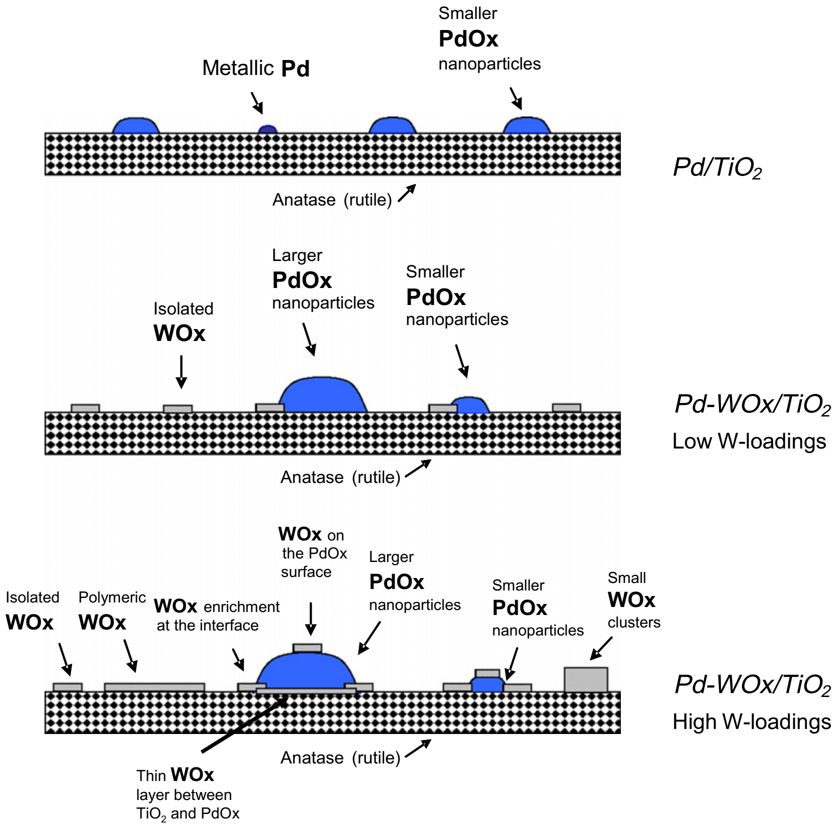

Fig. 17. Structural model of the $Pd/WO_x/TiO_2$ catalyst without addition of WO_x and with increasing WO_x loading.

active $0.5Pd/6W/TiO_2$ catalyst. After use, the Pd^0/Pd^{2+} ratio was 45/55, showing a higher degree of reduced palladium.

Sub-ambient TPR data of the $Pd–WO_x/TiO_2$ catalysts show that the reduction of the palladium species takes place at lower temperatures with increasing both the tungsten and palladium loadings, and this correlates with the catalytic activity. However, there is no simple relationship between ease of palladium reduction and the activity of the catalysts, as the Pd/TiO_2 catalyst showed palladium reduction at a lower temperature than the tungsten-containing catalysts, but it has lower activity. The more facile reduction of the Pd/TiO_2 catalyst could be due to the presence of Pd^0 sites, which are absent in $Pd–WO_x/TiO_2$, and these facilitate chemisorption and dissociation of H_2. There does appear to be a correlation between the activity of the $Pd–WO_x/TiO_2$ catalysts and the magnitude of the low-temperature reduction feature (Table 3). The combination of palladium and tungsten species gives rise to a larger number of reducible sites than can be accounted for based on the maximum quantity from palladium alone. Hence, a range of new highly reducible sites are generated, and these have facile oxygen species associated with them. We consider that these facile oxygen species are responsible for the increased oxidation activity and postulate that they are created at the peripheral interface between the WO_x species and the oxidised palladium nanoparticles on the TiO_2 support.

Just as the presence of tungsten modifies the structure of palladium, it has also been observed that the presence of palladium affects the nature of the tungsten species. According to Raman spectroscopy data, more polymeric tungsten species are present on a palladium–tungsten catalyst than in a tungsten only catalyst with the same tungsten content. The characteristic vibrational band in the frequency range between 950 and *ca.* 1020 cm^{-1} is assigned to W=O stretching vibration. The positions of these bands shift to higher frequencies with increasing tungsten loading at a fixed palladium content. Hence, these results provide evidence for increasing polymerisation of the surface tungstate as the tungsten loading increases. However, the dispersion of tungsten, as corroborated by XPS, is excellent. The STEM data are in agreement as these indicate mainly the presence of isolated surface monotungstate and polytungstate species. The presence of palladium in palladium–tungsten catalysts led to a marginal improvement of the reducibility of the oxidised tungsten species that are not associated with palladium nanoparticles. However, we consider that this particular modification is not directly responsible for the improved catalytic performance, since WO_x, regardless of the way it is structured, presents a very low reactivity for propane total oxidation. Moreover, according to the TPR experiments, the most reducible isolated tungsten species in W/Pd catalysts exhibit reduction bands at 450–500 °C, which are temperatures much higher than those required for the complete conversion of propane, and indicate that these oxygen species are not particularly reactive.

The presence of tungsten also modified the structure of the palladium particles, as electron microscopy showed evidence for formation of larger epitaxial palladium oxide particles, which were not present without tungsten. The structural modification of the palladium oxide particles could have some influence on increasing activity, but the potential influence of the epitaxial orientation is unclear. For supported metal particles, it has been reported that epitaxial formation of particles, induced by interaction with a support, can result in strain between the oxidised metal particle and metal oxide support [39]. It is also recognised that strained metal nanoparticle surfaces have modified adsorption energies and activation energies for reaction that differ from unstrained particles [40]. Although these studies were focussed on supported metal nanoparticles, it is not unreasonable to expect that the activity of epitaxial palladium oxide particles may differ from particles that do not show epitaxy. However, not all the palladium oxide particles of the tungsten modified catalyst showed epitaxial orientation and there were many that did not demonstrate epitaxy, accordingly it is not possible to deconvolute the relative activity from each particle type.

However, we consider that the most crucial factor for the enhanced activity is associated with the interface between the supported WO_x species and the palladium particles. By correlating the structure observed from aberration-corrected STEM characterisation with catalytic activity data, we propose that the new WO_x-decorated interface between PdO_x and TiO_2 particles may be responsible for the enhanced catalytic activity in the co-impregnated catalysts. Supporting evidence for this is supplied from sub-ambient TPR studies, which identified an increased concentration of highly reactive oxygen species on the catalyst. Some further evidence for these species is also apparent from the XPS analysis of the used palladium–tungsten catalyst, as after steady-state operation there was an increase in reduced palladium species on the catalyst surface, indicating their lability to react with propane. The reactive oxygen species are thought to be important for the increased activity as palladium-based catalysts for hydrocarbon total oxidation are known to operate via a Mars-van Krevelen-type mechanism [12].

Based on the catalytic data and the detailed characterisation studies, we have been able to propose a model to describe the structure of the catalyst (Fig. 17). With and without tungsten, palladium oxide nanoparticles were highly dispersed, although they were on average slightly larger and had some epitaxial orientation when tungsten was present. At lower tungsten loadings, isolated tungstate and some polytungstate species were highly dispersed over the titania support. The concentration of polytungstate increased as the loading was increased, as did the coverage over the titania. Finally, there were some tungstate species present on the palladium oxide particles, and there was an increased concentration of oxidised tungsten species at the peripheral interface of the palladium oxide nanoparticles and the titania.

4. Conclusions

$Pd/WO_x/TiO_2$ catalysts show high activity for the total oxidation of propane, and the activity is significantly greater than equivalent catalysts that do not contain tungsten. This enhanced activity is not simply the result of the additive effect of active sites on the palladium and tungsten species, as WO_x presents very low activity for the total oxidation of propane. Hence, there is a synergistic relationship between palladium and tungsten, and it is proposed that this is due to highly active oxidation species that are formed at the peripheral interface between TiO_2, WO_x and PdO nanoparticles. It is also interesting that the presence of tungsten induces epitaxial orientation in palladium nanoparticles. At present, a relationship between this epitaxial orientation and the high catalytic activity can be neither demonstrated nor excluded, and the effect is worthy of further study.

Acknowledgments

Authors wish to thank the Ministry of Science and Innovation (Spain) and the Generalitat Valenciana through Projects CTQ2009-14495 and GVPRE2008/352 for funding. C.J.K. is grateful to the NSF for funding provided under the Materials World Network Program (Grant # DMR-0709887).

References

[1] R.E. Heyes, S.T. Kolazkowski, Introduction to Catalytic Combustion, Gordon and Breach, Amsterdam, 1997.
[2] Q. Liu, L.-C. Wan, M. Chen, Y. Cao, H.-Y. He, K.-N. Fan, J. Catal. 263 (2009) 104–113.
[3] N.A. Merino, B.P. Barbero, P. Ruiz, L.E. Cadus, J. Catal. 240 (2006) 245–257.
[4] R.B. Anderson, K.C. Stein, J.J. Feenan, L.J.E. Hofer, Ind. Eng. Chem. 53 (1961) 809–812.
[5] S. Specchia, E. Finocchio, G. Busca, P. Palmisano, V. Specchia, J. Catal. 263 (2009) 134–145.
[6] T. Garcia, B. Solsona, S.H. Taylor, Catal. Lett. 97 (1–2) (2004) 99–103.
[7] A. Brayner, D.S. Cunha, F. Bozon-Verduraz, Catal. Today 78 (2003) 419–432.
[8] T. Garcia, B. Solsona, D.M. Murphy, K.L. Antcliff, S.H. Taylor, J. Catal. 229 (2005) 1–11.
[9] Y. Yazawa, H. Yoshida, N. Takagi, S. Komai, A. Satsuma, T. Hattori, J. Catal. 187 (1999) 15–23.
[10] K. Eguchi, H.i. Arai, Appl. Catal. A 222 (2001) 359–367.
[11] H. Bosch, F. Janssen, Catal. Today 2 (1998) 369.
[12] T.V. Choudhary, S. Banerjee, V.R. Choudhary, Appl. Catal. A 234 (2002) 1–23.
[13] K.-I. Fujimoto, F.H. Riberio, M. Avalos-Borja, E. Iglesia, J. Catal. 179 (1998) 431–442.
[14] C.A. Müller, M. Maciejewski, R.A. Koeppel, R. Tschan, A. Baiker, J. Phys. Chem. 100 (1996) 20006–20014.
[15] T.E. Hoost, K. Otto, Appl. Catal. A 92 (1992) 39–58.
[16] M. Vassileva, A. Andreev, S. Dancheva, N. Kotsev, Appl. Catal. A 49 (1989) 125–141.
[17] P. Papaefthimiou, T. Ioannides, X.E. Verykios, Appl. Catal. B 15 (1998) 75–92.
[18] P. Papaefthimiou, T. Ioannides, X.E. Verykios, Appl. Therm. Eng. 18 (1998) 1005–1012.
[19] F.B. Noronha, D.A.G. Aranda, A.P. Ordine, M. Schmal, Catal. Today 57 (2000) 275–282.
[20] A. Törncrona, M. Skoglundh, P. Thormählen, E. Fridell, E. Jobson, Appl. Catal. B 14 (1997) 131–145.
[21] P.O. Thevenin, A. Alcalde, L.J. Pettersson, S.G. Järås, J.L.G. Fierro, J. Catal. 215 (2003) 78–86.
[22] G. Pecchi, P. Reyes, T. López, R. Gómez, J. Non-Cryst. Solids 345–346 (2004) 624–627.
[23] M. Taylor, E. Ntainjua N., T. Garcia, B. Solsona, A.F. Carley, S.H. Taylor, Appl. Catal. A 350 (2008) 63–70.
[24] H.P. Klug, L.E. Alexander, X-Ray Diffraction Procedures, Wiley, New York, 1967.
[25] J. Engweiler, J. Harr, A. Baiker, J. Catal. 159 (1996) 259–269.
[26] M.H. Lee, B.C. Choi, J. Am. Ceram. Soc. 74 (1991) 2309.
[27] J.C. Parker, R.W. Siegel, J. Mater. Res. 5 (1990) 1246.
[28] H.C. Choi, Y.M. Jung, S.B. Kim, Vib. Spectrosc. 37 (2005) 33.
[29] G.C. Bond, S. Flamerz, L. van Wijk, Catal. Today 1 (1987) 229–243.
[30] S. Eibl, B.C. Gates, H. Knözinger, Langmuir 117 (2001) 107.
[31] D. Vermaire, P. Van Berge, J. Catal. 116 (1989) 309–317.
[32] G. Chen-Bin, L. Hung-Kuan, H. Chi-Man, J. Mol. Catal. A 180 (2002) 285–291.
[33] T. Kim, A. Burrows, C.J. Kiely, I.E. Wachs, J. Catal. 246 (2007) 370–381.
[34] X.-L. Yang, W.-L. Dai, Guo, H. Chen, Y. Cao, H. Li, H. He, K. Fan, J. Catal. 234 (2005) 438–450.
[35] W. Zhou, E.I. Ross-Medgaarden, W.V. Knowles, M.S. Wong, I.E. Wachs, C.J. Kiely, Nat. Chem. 1 (2009) 722–728.
[36] W. Zhou, I.E. Wachs, C.J. Kiely, Curr. Opin. Solid State Mater. Sci. (2011), doi:10.1016/j.cossms.2011.06.00.
[37] T.R. Baldwin, R. Burch, Appl. Catal. A 66 (1990) 337–358.
[38] R.F. Hicks, H. Qi, M.L. Young, R.G. Lee, J. Catal. 122 (1990) 295–306.
[39] N. Barrabés, K. Föttinger, A. Dafinov, F. Medina, G. Rupprechter, J. Llorca, J.E. Sueiras, Appl. Catal. B 87 (2009) 84–91.
[40] M. Mavrikakis, B. Hammer, J.K. Nørskov, Phys. Rev. Lett. 81 (1998) 2819.